China Instrument and Control Society
Instrumentation

OPEN ACCESS

INSTRUMENTATION, Vol. 11, No. 4, December 2024 https://doi.org/10.15878/j.instr.202400190

Article

Realizing Force Sensing with InGaN/GaN Multi-Quantum Well Diode Chip

Feifei Qin[1*], Jiaqi Wu[1], Shun Lu[2], Xueyao Lu[1], Yang Chen[1], Xumin Gao[1], Yue Cao[1], Lei Zhang[1], Xiaoxuan Wang[3*], Peng Wan[4], Gangyi Zhu[1], Yongjin Wang[1*]

[1] GaN Optoelectronic Integration International Cooperation Joint Laboratory of Jiangsu Province, College of Telecommunications and Information Engineering, Nanjing University of Posts and Telecommunications, Nanjing 210003, China

[2] Chongqing Institute of Green and Intelligent Technology, Chinese Academy of Sciences, Chongqing 400714, China

[3] State Key Laboratory of Digital Medical Engineering, School of Biological Science and Medical Engineering, Southeast University, Nanjing 210096, China

[4] College of Physics, MIIT Key Laboratory of Aerospace Information Materials and Physics, Key Laboratory for Intelligent Nano Materials and Devices, Nanjing University of Aeronautics and Astronautics, Nanjing 211106, China

[*] Corresponding author email: qinfeifei@njupt.edu.cn, wxxseu@seu.edu.cn, wangyj@njupt.edu.cn

Abstract: Force sensing provides a crucial physical-electrical channel within sensing technology. This study showcases the fabrication and characterization of force sensors by integrating a polydimethylsiloxane (PDMS) mechanical module and an optical channel formed by two ideal InGaN/GaN light-emitting diodes (LEDs) with transmit-receive characteristics. As an emitter, the InGaN/GaN device (5 mm×4 mm) exhibits electroluminescence at 469 nm with an on-voltage of 2.33 V. As a receiver, the response spectrum of InGaN/GaN devices spans from 350 to 480 nm, featuring a peak at 390 nm, rise time of ~68.4 ms, and falling edge of ~61.0 ms. The PDMS film can transform the force into deformation data and influence the signals in the optical receiver. The drive current, the gap between the emitter and receiver, and distance between the LED and PDMS mechanical module all significantly influence the receiver photocurrent. Distinct from the integrated design, our PDMS-assisted force sensing model uses discrete structures to allow signal intensity optimization. The finite element simulation and experimental results indicate that force of the designed PDMS film exhibits a linear relationship with z-axis displacement and photocurrent from 0 to 0.7 mm. The findings reveal that when the PDMS film height is 1.5 mm and the distance between the emitter and receiver is near, the photocurrent is higher. Meanwhile, Ag film with a thickness of 100 nm considerably enhances the photocurrent response and signal stability in the sensing channel. Finally, a weight measurement demonstration is employed to demonstrate force sensing. The system resolution is 1.23 μA/N, and the measurement range is 0 to 0.7 N.

Keywords: InGaN/GaN diodes chip; force sensing; coexistence of light emission and detection; PDMS

Citation: Feifei Qin, Jiaqi Wu, Shun Lu, Xueyao Lu, Yang Chen, Xumin Gao, Yue Cao, Lei Zhang, Xiaoxuan Wang, Peng Wan, Gangyi Zhu, Yongjin Wang. "Realizing Force Sensing with InGaN/GaN Multi-Quantum Well Diode Chip." Instrumentation 11, no. 4 (December 2024). https://doi.org/10.15878/j.instr.202400190

1 Introduction

Force parameters play an important role in intelligent robots, biomedical applications, materials science, and dimension measurements[1,2]. Many strategies have been proposed to realize force or pressure sensing in recent years. The operating principle of widely used force sensors is usually based on piezoelectric[3,4], magnetic[5,6], and capacitive[7-9] mechanisms. Piezoelectric force sensors usually have an edge in terms of cost, linear response and sensitivity, and piezoelectric sensors effectively convert dynamic forces to electrical signals by the direct piezoelectric effect. On the other side, a common charge of the neutralized surface makes it face some challenges in measuring static forces. [10] Magnetic force sensors operate with Lorentz force. The sensors commonly have a compact structure, wide measurement range, low energy consumption, high sensitivity and suitable performance. But the operating temperature has a great influence on this type of sensor, so it is necessary to add additional temperature compensation circuitry[6]. Meanwhile, capacitive sensors utilize the change in capacitance caused by external conditions as the input. Similar to magnetic force sensors, capacitive force sensors are also extremely sensitive to conditions such as temperature and humidity; their accuracy is not outstanding because it is more difficult to measure capacitance compared to resistance. All the above-mentioned devices can measure force levels from mN to pN[11]. Compared to the above-mentioned typical force sensors, a force sensing system based on optical methods is more accurate and easier to realize. Optical force sensors usually contain a mechanical unit and a signal acquisition system with a light source and a photodetector or an optical spectrometer. The discrete device structure provides the optical force sensor system great freedom in terms of component selection and parameter optimization, and it is usually more inexpensive. For example, Uzun *et al.* prepared an optical force sensor that showed an enhanced resolution of 0.03 N from 0 to 20 N with the Fabry-Pérot Interferometry (FPI) method[12]. Leal-Junior *et al.* presented the development of a bioinspired multifunctional flexible optical sensor (BioMFOS) as an ultrasensitive tool for force (intensity and location) and orientation sensing[13]. This sensor allows the measurement of μN-level forces and the reconstruction of the shape of forces applied on the sensor with sub-millimeter spatial resolution. Although this force sensing system has seen great success, multifunctional devices are urgently needed for achieving miniaturization and integrating sensing units; consequently, they can be used to improve the device performance further.

Recently, InGaN/GaN-based multi-quantum wells (MQWs) have been widely researched for use in light-emitting diodes (LEDs) [14, 15], with applications in lighting, displays, communication devices, etc[16-18]. These LEDs exhibit good thermal stability; they are prone to structural degradation at temperatures higher than 900° C, which affects their normal operation. Therefore, devices based on these LEDs can work normally under non-extreme temperature conditions. Since both the emitter and detector co-exist in MQW-based devices, they also function as bi-functional optoelectronic devices that can simultaneously emit, detect, and modulate light[19-21]. These multi-function devices have also been used in sensing applications. For example, Liu *et. al* reported a fully integrated patch based on lamellar porous film-assisted GaN optopairs for wireless intelligent respiratory monitoring[22]. Our previous work also presented a chip-integrated optical fiber magnetic field sensing system based on GaN MQWs[23]. More importantly, since the transceiver integration is an inherent property of any GaN LED device with MQW structure, the design of the optical sensor system can also be built with commercialized LED, the cost of the entire system can be compressed to several dollars or less, and it is expected to be applied to disposable replaceable sensing units.

In this work, we designed and fabricated a force-sensing unit by combining an Ag-decorated polydimethylsiloxane (PDMS) mechanical module with an optical channel formed by two ideal InGaN/GaN LEDs. In our design, one LED acts as the emitter and the other as the receiver, thereby forming a sensing path. Meanwhile, the PDMS film functions as a receiver, transforms the pressure into displacement, and eventually generates the photocurrent in the LED. The separation design of the electrical signal unit and the mechanical sensing unit gives the force sensor device significant optimization freedom. The mechanical properties of the PDMS film have been studied using experiments and finite element simulation. The photocurrent properties of the proposed devices are optimized by introducing Ag film, varying the distance between the emitter and receiver, and altering the distance between the LED and PDMS film. Finally, the force-sensing properties of the system are studied.

2 Experiments section

2.1 Fabrication of the InGaN/GaN LED Chip

Similar to our previous work[24], the sample in this study was fabricated using a standardized device process, which involves photolithography and inductively coupled plasma (ICP) etching on a four-inch and 6.2 μm thick sapphire-based GaN film. From top to bottom, the epitaxial film contains Mg-doped p-GaN, InGaN/GaN MQW, Si-doped n-GaN, and unintentionally doped GaN (u-GaN), and their thicknesses are 0.4 μm, 0.35 μm, 2.8 μm and 1.5 μm, respectively. For the device fabrication process, a mesa region was defined via photolithography and ICP etching to expose the n-GaN surface. A deep ICP etching was then performed to obliterate epitaxial films for device isolation (Steps a-b). Then, a transparent indium tin oxide (ITO) current spreading layer with a thickness of 230 nm was deposited via sputtering, which was followed by rapid thermal annealing at 530^{o}C in N_2 atmosphere (Steps b-c).

Subsequently, the ITO layer was patterned and etched with a mixture of $HCl/FeCl_3$ solution to expose n-GaN. Then, the surface electrode was subjected to a metal lift-off process and metal stacks subjected to rapid thermal annealing (850° C, 30 s, and N_2 atmosphere) were deposited on the n-GaN and reflector (DBR) containing 36 pairs of SiO_2/TiO_2 on the bottom sapphire surface of the LED (Steps d-e). Finally, a square LED with a size of 5×4 mm was prepared (Figure 1f). Subsequently, a comb-like surface electrode was introduced into the device to improve current uniformity. The generated current allows the entire LED to be lit (Figure 1g).

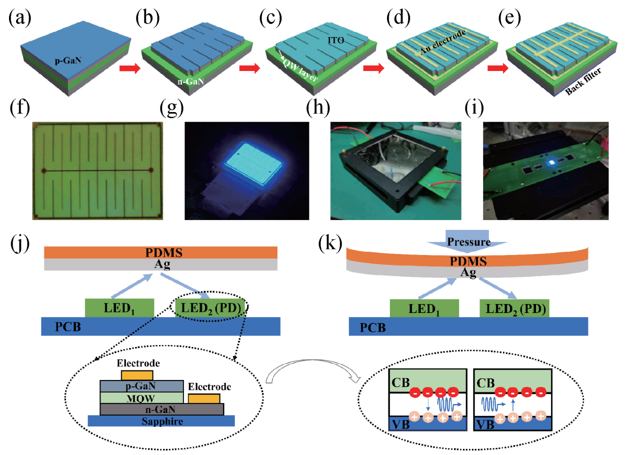

Fig.1 (a–e) Schematic of the sample preparation process of In GaN/GaN MQW devices. Optical images of the actual sample (f), luminous photograph (g), and physical view of the sensing module (h,i). Schematic depicting the principle of the sensing unit (j,k), the inset shows the materials and energy band structure of the LEDs.

2.2 Fabrication of the PDMS/Ag film

The PDMS/Ag multi-film used in our work was fabricated via electron beam evaporation. In this process, a 100 nm Ag film was deposited on a commercial PDMS film (10×10 cm in size and 50 μm in thickness) at a rate of 0.1 nm/s. The top-view optical images of PDMS before and after Ag deposition are shown in Figure S1. The pure PDMS film is transparent, and the Ag particle can be seen clearly in the PDMS/Ag film. This particle blocks the light transport properties and augments the reflected signal in sensing applications.

2.3 Design of the force sensing unit

Figure 1(h, i) shows that the sensing module is built by placing the PDMS/Ag film in a designed holder as the mechanical sensing element, while two separated InGaN/GaN photonic chips are made to bond with a printed circuit board (PCB) substrate and function as the signal transform unit. The discrete device structure ensures flexible distance control. The luminescence and detection structures in LED_1 and LED_2 can help the device switch between the emitter and receiver. Overall, the above-mentioned features will benefit further optimization of the sensing properties. The principle of the signal transform unit is shown in Figure 1(j,k). The emitter and receiver are placed behind the PDMS/Ag film. In the absence of pressure (Figure 1(j)), the light produced by LED_1 is reflected by the PDMS/Ag film, received by LED_2, and transformed into a stable photocurrent. If the PDMS/Ag film is subjected to any form of pressure, a strain is produced and the distance between the PDMS/Ag film and the two LEDs increases. Consequently, the photocurrent of LED_2 changes. The working principle of the mechanical module is shown in Figure 2(a); within the elastic deformation range, the device can be used as a strain gauge-based force sensor[25]. The force or pressure imposed on the device tends to change the shape of the PDMS film. To further demonstrate the working principle of the mechanical module, a simulation was performed

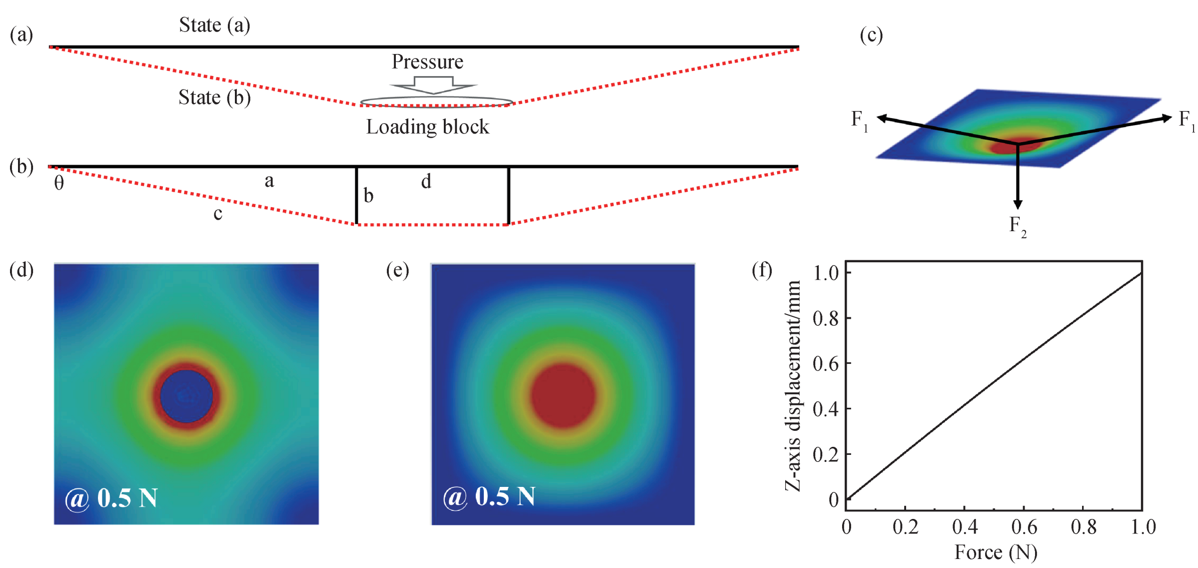

Fig.2 (a) Simplified mechanical model for the mechanical sensing elements, (b) physical parameters of the mechanical sensing elements under force, and (c) force analysis. Simulation results of (d) tensile stress and (e) z-axis displacement distribution in the polymer membrane under 0.5 N, and (f) relationship between force and normalized z-axis displacement.

based on finite element methods. Figure 2 (a, b) shows that when the PDMS/Ag multi-film is subjected to pressure, it undergoes a change from state a to state b. According to the classic Hooke's law, the stress can be expressed as follows[1]:

$$\sigma = \frac{F}{A_0} = E\epsilon = E\frac{\Delta L}{L} \tag{1}$$

where E is Young's modulus of the material, A_0 is the cross-section area, ϵ is the strain, L is the length of the material, and ΔL represents the changes in material length. The PDMS film which has a size of 90 mm× 90 mm was used in our experiment and the diameter of the block is 18 mm. During the stress analysis, the length in the z-direction is 1 mm; thus, a = 36 mm, d = 18 mm, and b ranges between 0 and 1 mm. The change in the length of the PDMS film can be calculated as follows:

$$\Delta L = \sqrt{a^2 + b^2} - a \tag{2}$$

When pressure is applied to the PDMS film with the experimental device shown in Figure S2, the angle change induced in its shape is defined as follows:

$$\sin\theta = b/\sqrt{a^2 + b^2} \tag{3}$$

Based on the mechanical analysis in Figure 2(b), the equivalent vertical force F_2 is expressed in Figure 2(c):

$$F_2 = 2F_1\sin\theta \tag{4}$$

Based on Eq. 1-4 and the parameters shown in Figure 2(b), the relationship between the pressure or force and the change in the PDMS film can be obtained. Besides, the force can hold a linear relationship with the sharp changes of PDMS film in a small θ degree, and the relationship will change for a big θ degree. Normally, the sharp changes will be the function of Young's modulus and Poisson's ratio. A simulation is performed by selecting the Young's modulus as 750 kPa and Poisson's ratio as 0.49 for the PDMS film, the Ag film thickness as 100 nm, and the PDMS film thickness as 50 μm. The simulation results in Figure 2(d, e) imply that strain is mainly distributed on the central portion of the PDMS film, which causes a displacement in the z-direction. As expected, with increasing pressure, normalized displacement increases linearly in the force region of 0–1 N (Figure 2(f)). By monitoring the reduced changes in photocurrent, the force-sensing properties of our device can be obtained. Moreover, since the LEDs have the same structure as that of InGaN/GaN multiple quantum wells (MQWs), the coexistence of light emission and detection in this design can ensure that each LED serves as both the emitter and photodetector (PD)[26]. The LED can receive light from the other LED nearby and once the sensing channel is formed, the receiver and emitter can be interchanged.

3 Results and discussion

3.1 Luminescence and detection characteristics of the InGaN/GaN LED

Electroluminescence (EL) and photodetector properties of the InGaN/GaN LED are essential for preparing sensing devices. Figure 3(a) shows that the

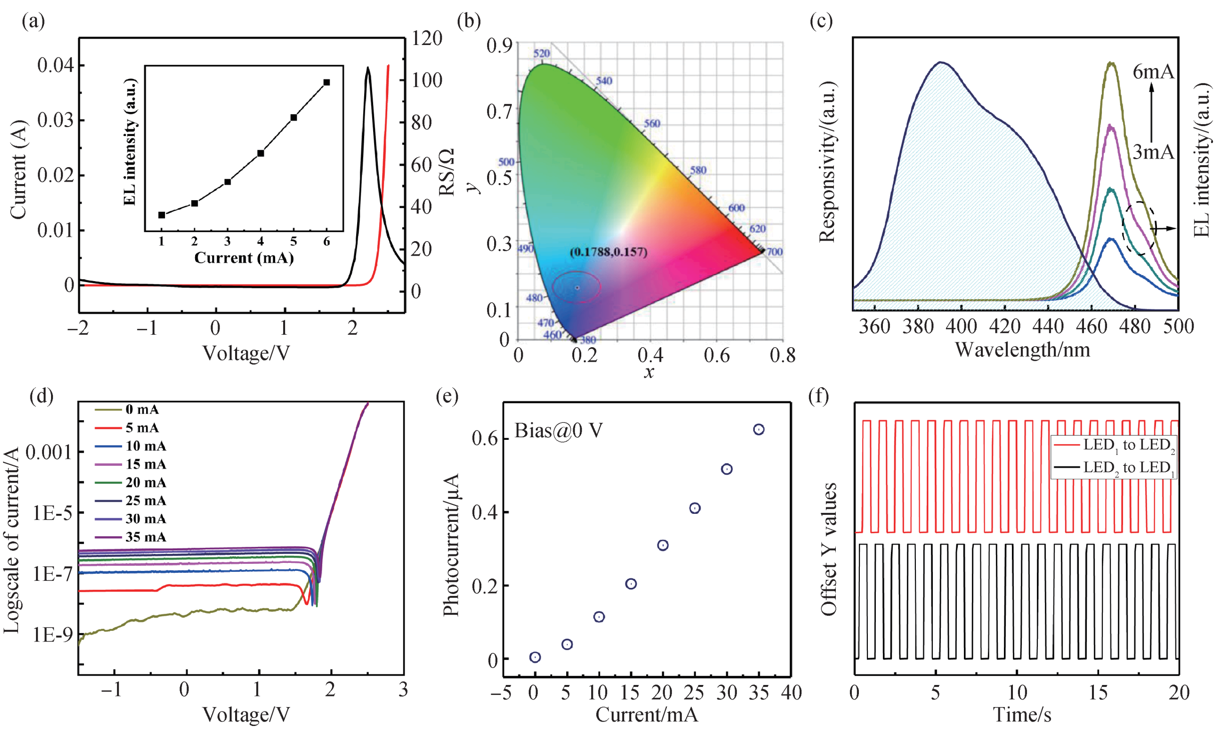

Fig.3 EL properties of InGaN/GaN LED as an emitter: (a) Current-voltage (IV) and impedance characteristics; inset shows the driven-current related EL intensity. (b) Coordinates of the CIE 1931 chromaticity diagram. (c) Driven current-related EL spectra and normalized spectral sensitivity. (d) PD properties of InGaN/GaN LED as the receiver: (d) IV curves and (e) photocurrent variation with different LED currents. (f) Dynamic photocurrent response of the MQW-PD with emitter and receiver.

current-voltage (I-V) properties of the individual InGaN/GaN LED have been measured using an enhanced Keithley source meter (B2901 of 100 fA). The turn-on voltage is ~2.33 V and the resistance is 106 Ω (Figure 3(a)). EL spectra of the sample were measured with a spectrograph (Acton SP2500i). The broad spectra of the InGaN/GaN LED peaks at 469 nm, while the full width at half maximum (FWHM) is 19.5 nm and the chromaticity coordinates are (0.1788, 0.157) in the CIE 1931 chromaticity diagram (Figure 3(b, c)). The EL intensity increases after a driven current is added (Figure 3(a) inset).

Optical response spectra of the InGaN/GaN device as a PD are shown in Figure 3(c). The device exhibits a light response in the 350 to 480 nm region, which decreases as the receiver is measured under light irradiation provided by the nearby LED. Without light irradiation, the dark gradually for incident light. The overlap between EL and response spectra (~40 nm) is key to realizing a sensor with a transceiver integrated chip[27, 28]. IV curves of a single device photocurrent are in the nA range (Figure 3(d)). The photocurrent increases with a rise in the driven current of LEDs nearby. The photocurrent increases to μA levels under light illumination. When the driven current ranges from 0 to 35 mA, photocurrent increases linearly at a bias voltage of 0 V (Figure 3(e)). Thus, we used a bias voltage of 0 V for further experiments. The dynamic photocurrent response of the proposed LED and PD channel is shown in Figure 3(f). Given that LED_1 and LED_2 exhibit the same device structure, the signals they produce are nearly identical with regard to response speed and signal strength. The reproducibility and stability of the device were evaluated via cyclic testing (Figure 4(a)). The output photocurrent signals remain remarkably stable for 200 s, which is equivalent to over 100 cycles. Subsequently, we further extended the testing time and tested the stability and reliability of the signal which lasted for about 30 minutes. The error range obtained was within ±1%, as shown in Figure S3. The transient photo-response in Figure 4(b) shows the recovery time, which is defined as the time required for the increase in photocurrent to drop from 90% to 10%; the rise time is ~68.4 ms and downtime is ~61.0 ms. Although the recovery time is slower than other sensors, it is fast enough for steady-state sensing applications[29].

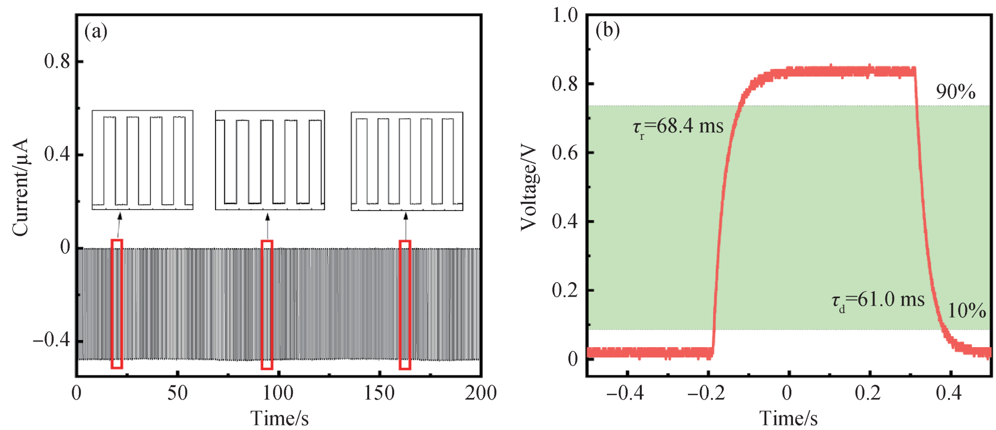

Fig.4 (a) Dynamic photocurrent response of the MQW-PD over 100 cycles. (b) Instantaneous response of the device.

3.2 Parameter optimization for the signal transform unit

Issues such as the driven current of the LED, the space between the LEDs and PDs, and the gap between the mechanical module and electrical module may influence the sensing performance of the device. To figure out it, Figure 5 shows how different variables affect the sensor's detection performance, which ultimately includes the distance between the two LEDs, the distance between the detection structure and the physical structure, and whether a silver-modified PDMS film is used. Define D as the gap between the emitter and receiver and H as the height between the PDMS film and LEDs pairs. For samples with Ag in Figure 5(a), the photocurrent decreases with the addition of H values. For a fixed driven current of 10 mA for the emitter, photocurrents of the receiver at different D values and H values are shown in Figure 5(b, c). The sample without Ag film exhibits a photocurrent value of 415 nA to 10.5 nA when its thickness ranges from 1.5 to 6 mm and the spacing region ranges between 0 and 30 mm (Figure 5 (b)), current decreases with the addition of D values but no obvious regular can be seen for the changes of H values. The photocurrent ranges from 1.74 μA to 40 nA for samples with a Ag film when its thickness ranges from 1.5 to 6 mm and the spacing region ranges between 0 and 30 mm (Figure 5(c)). The photocurrent decreased with the addition of H and D values. Besides, the photocurrent is enhanced because the Ag film augments the light reflected by the PDMS film and the signal is more stable. To further demonstrate this, we simulated the electromagnetic field via FDTD simulation (see details of the simulation methods in the supporting information). Figure 5(d) shows that the PDMS film with an Ag film has a higher electromagnetic field. All these

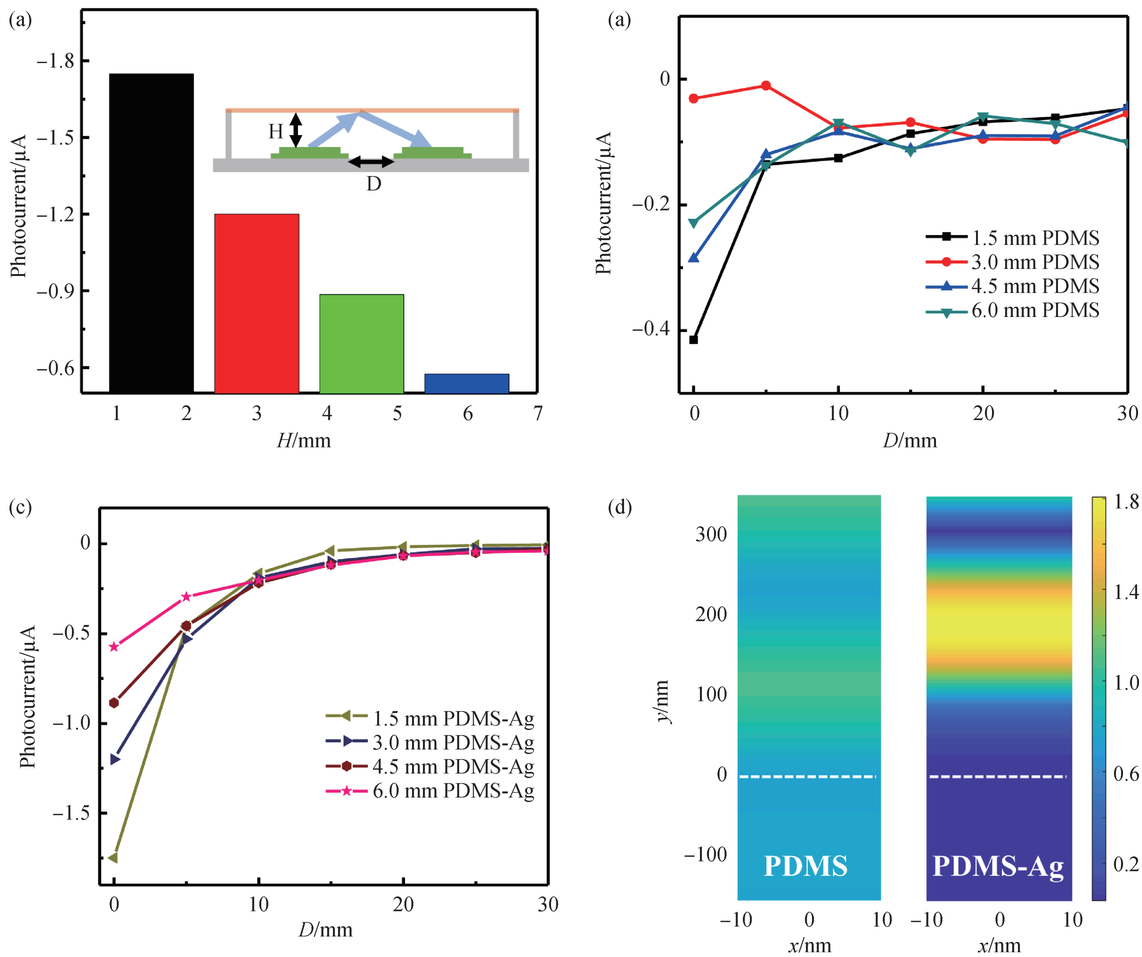

Fig.5 (a) Photocurrent of PD at different heights between the LED and PDMS-Ag film. Photocurrents vary with the space between the LED and PD: (b) without Ag film, (c) with Ag film. (d) Electromagnetic field distribution of the PDMS film with or without Ag.

results indicate that the sample with an Ag film, which is placed near the emitter and receiver and between the PDMS film and LEDs, will have a higher sensing signal. Thus, we chose D as 0 mm and H as 1.5 mm for subsequent force sensing experiments.

3.3 Demonstration of the force sensing system

Based on the experimental setup of Figure 1(j, k), the force sensing system is built. The applied force was analyzed by transforming the shape change of the PDMS film into the photocurrent of InGaN/GaN LEDs. With the optimized parameters, a real force sensing system was constructed (Figure 6 (a−c)). By adding a weight to the PDMS film, different photocurrents are observed. The photocurrents increase linearly when the force varies from 0 N to 0.7 N at a sensitivity of 1.23 μA/N (Figure 6 (d)). Subsequently, we conducted repetitive tests for force-related photocurrent under various lighting conditions to verify the experiment's robustness, and determined that the standard deviation of the system's sensing performance was within 30-49 nA, as shown in the supplementary material (Figure S4). To further demonstrate the sensing properties, the fatigue tests and shape changes induced sensing properties were verified. Based on the schematic shown in Figure 6 (e, f), sharp changes induced photocurrent of the device were performed with a stepper motor that controls the block (see picture of real products in Figure S2) with a move region of 0 to 1 mm. For each position in Figure 6 (g), photocurrent increases linearly from 0 to 0.7 mm and remains stable for the next 0.3 mm. This phenomenon is similar to the observations made after weights were placed on top of the sensor (Figure 6(d)); the results confirm the working principle of our system. Figure 6(h) displays the measurement results of the sensor for cyclic tests; As expected, the photocurrent is increased then stable and then decreased with the times. The photocurrent profiles imply high stability over 150 cycles. As shown by the transient response of the sensor in Figure 6(i), the photocurrent remains stable with increasing time and then rises linearly with time.

To demonstrate the advantages of our sensor, we compared its parameters with those of some existing sensors, including sensitivity, measurement range, and response time; the response time was replaced with the rise time. The comparison reveals that our sensors exhibit good sensitivity and response speed. The response time is better than most other sensors in the comparison. However, it has a smaller range than other sensors.

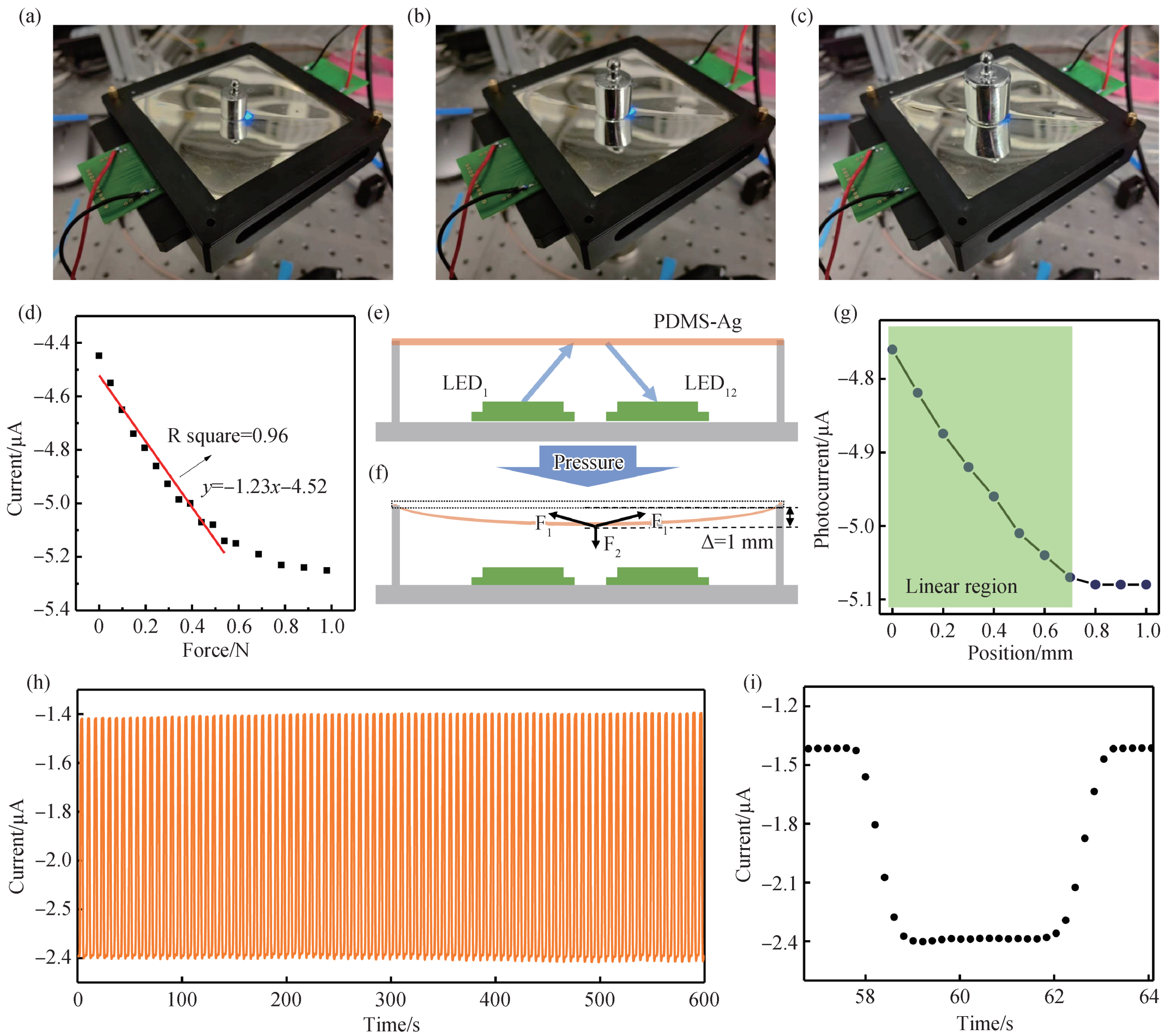

Fig.6 (a-c) Pictures of the device with different weights, (d) force-related photocurrent, (e, f) simplified system diagram for fatigue tests, (g) position-related photocurrent, (h) cyclic measurement of the sensor over 150 cycles, and (i) transient response of the sensor.

Table 1 Comparison of the optic force sensor and previously reported ones

Sensor type	Sensing medium	Sensitivity (kPa^{-1})	Range (kPa)	Rise time
This work	Ag-modified PDMS	0.320	0~2.23	68.4 ms
Capacitive flexible sensor[30]	PDMS/$BaTiO_3$/Sr TiO_3 dielectric layer	2.681	0~5	39 ms
Capacitive resistance composite sensor[31]	PPy filter	0.186	0~23	1.5 s
Iontronic flexible sensor[32]	PBST nanofiber membranes	902.4	0~6	147 ms
Resistance sensor[33]	PDMS-Silicon nanofilms	0.0023	0~200	85 ms

4 Conclusion

In this study, a force sensor with two separated InGaN/GaN photonic chips function as the signal transform unit and a designed PDMS holder acts as the mechanical sensing element has been fabricated. The LEDs are functioned as both the emitter and receiver. As an emitter, the turn-on voltage, EL peak, and FWHM of the device are 2.33 V, 469 nm, and 19.5 nm, respectively. As a receiver, the photoresponse spectra peaked at 390 nm with a cut-off wavelength of 480 nm and a falling edge of 61.0 ms. The Ag/PDMS multi-film was fabricated by depositing a 100 nm thick Ag film on a commercial PDMS film to function as the mechanical module. The multi-film was attached to a homemade holder to fabricate a force-sensing device. The light produced by the emitter is reflected back to the receiver by the PDMS film, and the signal strength is increased by the Ag film in a linear region of 0-0.7 mm. Within the elastic deformation range, the variations in the force applied to the PDMS film were transformed into the photocurrent and force sensing was achieved. The gap between the emitter and receiver and the distance between the mechanical module and signal transform unit can influence the performance of the device. Our results indicate that the photocurrent is higher when the PDMS film has a height of 1.5 mm and the emitter and receiver are close to each other. Finally, force sensing was demonstrated using weights, and a system resolution of 1.23 μA/N was achieved from 0 to 0.7 N.

Author Contribution:

Feifei Qin: Conceptualization, Methodology, Writing original draft. Jiaqi Wu: Testing, Simulation, Writing original draft. Shun Lu: Writing - review & editing. Xueyao Lu: Hardware. Yang Chen: Software. Xumin Gao: Testing. Yue Cao: Data Curation. Lei Zhang: Formal analysis. Xiaoxuan Wang: Conceptualization. Peng Wan: Testing. Gangyi Zhu: Data collection. Yongjin Wang: Project adminstration.

Funding:

This work is supported by the Natural Science Foundation of Jiangsu Province (BK20210593), the National Natural Science Foundation of China (62204127, 62404040), and the Fundamental Research Funds for the Central Universities (No. NS2022096).

Supporting documents

Supporting information for size details of PDSM, physical diagram of pressure test device, data stability testing and numerical simulation methods.

Dates:

Received 30 May 2024; Accepted 17 November 2024; Published online 31 December 2024

References

[1] WEI Y, XU Q. An overview of micro-force sensing techniques [J]. *Sensors and Actuators A: Physical* , **2015**, 234: 359-74.

[2] ROTHMAIER M, LUONG M P, CLEMENS F. Textile pressure sensor made of flexible plastic optical fibers [J]. *Sensors* , **2008**, 8(7): 4318-29.

[3] KIM K, KIM J, JIANG X, et al. Static force measurement using piezoelectric sensors [J]. *Journal of Sensors* , **2021**, 2021: 1-8.

[4] CURRY E J, KE K, CHORSI M T, et al. Biodegradable piezoelectric force sensor [J]. *Proceedings of the National Academy of Sciences* , **2018**, 115(5): 909-14.

[5] HUNG C-F, YEH P-C, CHUNG T-K. A miniature magnetic-force-based three-axis AC magnetic sensor with piezoelectric/ vibrational energy-harvesting functions [J]. *Sensors* , **2017**, 17 (2): 308.

[6] HERRERA-MAY A L, SOLER-BALCAZAR J C, VáZQUEZ-LEAL H, et al. Recent advances of MEMS resonators for Lorentz force based magnetic field sensors: design, applications and challenges [J]. *Sensors* , **2016**, 16(9): 1359.

[7] YAO T, GUO X, LI C, et al. Highly sensitive capacitive flexible 3D-force tactile sensors for robotic grasping and manipulation [J]. *Journal of Physics D: Applied Physics* , **2020**, 53(44): 445109.

[8] PENG S, WU S, YU Y, et al. Multimodal capacitive and piezoresistive sensor for simultaneous measurement of multiple forces [J]. *ACS applied materials & interfaces* , **2020**, 12(19): 22179-90.

[9] NASTRO A, FERRARI M, FERRARI V. Double-actuator position-feedback mechanism for adjustable sensitivity in electrostatic-capacitive MEMS force sensors [J]. *Sensors and Actuators A: Physical* , **2020**, 312: 112127.

[10] KIM K, KIM J, JIANG X, et al. Static Force Measurement Using Piezoelectric Sensors [J]. *Journal of Sensors* , **2021**.

[11] BROOKHUIS R A, LAMMERINK T S, WIEGERINK R J, et al. 3D force sensor for biomechanical applications [J]. *Sensors and actuators A: physical* , **2012**, 182: 28-33.

[12] UZUN D, ÜLGEN O, KOCATüRK Ö. Optical force sensor with enhanced resolution for MRI guided biopsy [J]. *IEEE Sensors Journal* , **2020**, 20(16): 9202-8.

[13] LEAL-JUNIOR A, AVELLAR L, BIAZI V, et al. Multifunctional flexible optical waveguide sensor: On the bioinspiration for ultrasensitive sensors development [J]. *Opto-Electronic Advances* , **2022**, 5(10): 210098-1-11.

[14] ROCCATO N, PIVA F, DE SANTI C, et al. Modeling the electrical characteristics of InGaN/GaN LED structures based on experimentally-measured defect characteristics [J]. *Journal of Physics D: Applied Physics* , **2021**, 54(42): 425105.

[15] WANG Z, ZHU S, SHAN X, et al. Full-color micro-LED display based on a single chip with two types of InGaN/GaN MQWs [J]. *Optics Letters* , **2021**, 46(17): 4358-61.

[16] CHEN Z, SHENG B, LIU F, et al. High - Efficiency InGaN Red Mini-LEDs on Sapphire Toward Full-Color Nitride Displays: Effect of Strain Modulation [J]. *Advanced Functional Materials* , **2023**, 33(26): 2300042.

[17] GONZÁLEZ-IZQUIERDO P, ROCHAT N V, ZOCCARATO D, et al. Influence of shape and size on GaN/InGaN μLED light emission: A competition between sidewall defects and light extraction efficiency [J]. *ACS Photonics* , **2023**, 10(11): 4031-7.

[18] XU F, QIU P, TAO T, et al. High bandwidth semi-polar InGaN/GaN micro-LEDs with low current injection for visible light communication [J]. *IEEE Photonics Journal* , **2023**, 15(1): 1-4.

[19] ZHANG H, YAN J, YE Z, et al. Monolithic GaN optoelectronic system on a Si substrate [J]. *Applied Physics Letters* , **2022**, 121(18).

[20] YAN J, WANG L, JIA B, et al. Uniting GaN electronics and photonics on a single chip [J]. *Journal of Lightwave Technology* , **2021**, 39(19): 6269-75.

[21] LI J, WU J, CHEN L, et al. On-chip integration of III-nitride

flip-chip light-emitting diodes with photodetectors [J]. *Journal of Lightwave Technology* , **2021**, 39(8): 2603-8.

[22] LIU Z, SU J, ZHOU K, et al. Fully Integrated Patch Based on Lamellar Porous Film Assisted GaN Optopairs for Wireless Intelligent Respiratory Monitoring [J]. *Nano Letters* , **2023**, 23 (23): 10674-81.

[23] YE Z, ZHANG H, SHI F, et al. Chip-integrated optical fiber magnetic field sensing system [J]. *Optics Letters* , **2023**, 48 (21): 5659.

[24] QIN F, LU X, CHEN Y, et al. Concentration sensing system with monolithic InGaN/GaN photonic chips [J]. *Chinese Optics Letters* , **2024**, 22(6): 062501.

[25] CHOI W-C. Polymer Micromachined Flexible Tactile Sensor for Three-Axial Loads Detection [J]. *Transactions on Electrical and Electronic Materials* , **2010**, 11(3): 130-3.

[26] FU K, GAO X, YE Z, et al. Coexistence of light emission and detection in a III-nitride quantum well diode [J]. *Optics Letters* , **2022**, 47(11): 2614.

[27] YIN J, LUO Y, CHEN L, et al. High-Resolution Optical Three-Axis Tactile Microsensor Based on III-Nitride Devices with Integrated PDMS Bumps [J]. *IEEE Electron Device Letters* , **2023**, 44(12): 2035-8.

[28] FU J, FU K, YE Z, et al. Multichannel Visible Light Communication over a Single Optical Path [J]. *ACS Photonics* , **2023**.

[29] CHEN J, YIN J, AN X, et al. III-nitride microchips for sugar concentration detection [J]. *IEEE Sensors Journal*, **2021**, 22 (3): 2078-82.

[30] SUN H, CHEN S, XU C, et al. Flexible Capacitive Pressure Sensors with Porous Double-Microstructure Layer, Micronanoelectronic Technology, **2024**, 61(04): 111-119.

[31] SONG Y, HU Z, LI J, et al All-paper-based smart sensor for proximity-pressure perception. *Scientia Sinica Chimica* , **2024**, 54: 667-676.

[32] ZHAO M, LI F, CUI M, et al. *Preparation and Performance of All-nanofiber Iontronic Flexible Pressure Sensor Journal of Beijing Institute of Fashion Technology* , **2024**, 44(01): 55-64.

[33] CHEN L. Research on Flexible Pressure Sensor with Laminated Structure Based on PDMS-Nanomaterial **2023**. *10.27470/d.cnki.ghbgc.2023.000019* .